NLO QCD and EW predictions for $t\bar{t}$ and $t\bar{t}H$ production and decay at a Muon Collider

Francesco Pio Ucci, Dipartimento di Fisica, Università di Pavia, Italy

September 7, 2022

Abstract

The study of the top quark properties plays a crucial role in probing the Higgs sector and, possibly, suggesting hints for new physics. In this work presented predictions for on- and off-shell $t\bar{t}$ and $t\bar{t}H$ production at a future Muon Collider are presented, including next-to-leading-order QCD and EW corrections.

Contents

1. Introduction

As of today, particle physics is searching for new physics as well as trying to solve manifest problems of the Standard Model. In the context of the Standard Model (SM) the top quark is the most massive particle, hence the precision study of its properties plays a crucial role in probing the Higgs sector and, possibly, suggesting hints for new physics. Hence, colliders are suitable for both exploring new energy limits and doing precision tests of models. As current colliders are going to be pushed to the extreme of their capabilities, a new collider capable of investigating the future possible discoveries from the actual experiments as well as offering new opportunities for exploration is needed.
One proposal for a new collider is the Muon Collider [1]. It has the advantage of colliding fundamental massive particles, that is having the whole centre of mass energy available for the collision and overcoming the problem of synchrotron radiation for muon having ~ 200 times the mass of electrons.
At a muon collider quantities like the top quark mass, the forward-backward asymmetry or the top Yukawa coupling can be measured with increased precision. Is it so necessary to have accurate theoretical predictions for such processes at high perturbative orders.
In this work, the on-shell top-pair production and the top-pair production with an associated Higgs boson will be analysed. Following the path of the work [2], the NLO QCD corrections for those processes will be analyzed, extending the study also to EW NLO correction, where possible. Then predictions for the top Yukawa coupling and the forward backward asymmetry will be presented.
The used simulation environment is the WHIZARD Monte Carlo event generator, in association with the one loop matrix element generators OPENLOOPS and RECOLA.

2. Calculation setup

2.1. WHIZARD environment

All the calculations reported in this study are obtained via the WHIZARD Monte Carlo generator [3], [4], in association with the matrix element generators RECOLA [5] (for EW corrections) and OPENLOOPS (for QCD corrections). WHIZARD is a multi-purpose event generator, suitable both for hadron and lepton collider. It can be used for generating events at the parton level as well as handling the parton shower and hadronization with PYTHIA8. In this setup, the event generation is done at parton level, and the final state particles are assumed on-shell.
For NLO calculations, the integration in WHIZARD is done via the FKS subtraction method, which divides the phase space into single divergent regions, that is where only one divergent integral is present. The integration is carried out with a Vegas algorithm. The matrix element generation is done in four space-time dimensions, within the dimensional regularization scheme. The NLO matrix element generation is handled by OPENLOOPS for the QCD corrections and with RECOLA for the EW corrections. One

of the main differences between the two is that OPENLOOPS supports only massless leptons, while RECOLA can take into account the muon masses.
All QCD integrations, which are faster, are done with 10 iterations of 100000 calls each, both at leading and next-to-leading orders. For EW corrections, the NLO integration is done with only 10000 calls, because problems rise with higher numbers of calls. The number of generated events is 10^6 for each process, which is a fine order of magnitude but needs to be improved at least with a factor of 10, in order to reduce statistical fluctuations.
Calculations are parallelised via the `mpirun` routine on the theory cluster at DESY, with machines of 47 processors each.
The WHIZARD Monte Carlo generator is able to save data in multiple formats. The output chosen for this analysis is HEPMC, a common standard in both theoretical calculations and experimental studies. The output files are analysed via the RIVET2 [6] framework. This analysis tool is able to produce all the desired histograms, given a `C++` script where particles are identified via their PID and stored as Rivet Jets and histograms are filled with their properties. The output of the RIVET analysis is a YODA file, i.e. a text file that stores all the histograms data in columns and which can be plotted. For scale variations, the envelopes are produced with a custom `python` script, saved as a yoda file, which provides the error bars.

2.2. Renormalization scheme

Infrared and Ultraviolet divergences are regularized as poles in $4 - D$ space-time dimensions, within the standard dimensional regularization. However, the matrix element generation is carried out in four space-time dimensions, since the $4 - D$-dimensional terms are process-independent counterterms.
The strong running coupling is computed at the second order in the $\overline{MS}$ scheme, with $n_f = 5$ active flavours.
In all cross section and width calculations, the complex mass scheme CMS [7] [8] will be used, in which the intermediate particle masses are treated as complex quantities. In this scheme, masses are defined as the poles locations of the propagators with flowing momentum k in the complex k^2 plane. As unstable particles self energies are complex quantities, masses contain a complex part proportional to particles width, and read

$$\mu_i = M_i^2 - iM_i\Gamma_i, \qquad i = t, W, Z, H \tag{1}$$

To preserve gauge invariance, complex masses are consistently introduced in all Feynman rules. Hence the weak mixing angle is defined as

$$\cos^2\theta_W = c_w^2 = 1 - s_w^2 = \frac{\mu_W^2}{\mu_Z^2} \tag{2}$$

The model used is the SM with the (G_F, M_Z, M_W) scheme, taking as input the Fermi coupling $G_F = 1.166\,378\,7 \times 10^{-5}\,\mathrm{GeV}^{-2}$ and the vector boson masses, the electromag-

netic coupling value is given by

$$\alpha_e = \frac{\sqrt{2}}{\pi} G_F \left| \mu_W \sin\theta_W \right|^2$$

The strong coupling constant is taken at the Z-peak $\alpha_s(M_Z) = 0.118$ The renormalization scale for $t\bar{t}$ and $t\bar{t}H$ processes is chosen as

$$\mu_R = \xi_R \begin{cases} m_t & \text{for } t\bar{t} \\ m_t + \frac{m_H}{2} & \text{for } t\bar{t}H \end{cases}, \qquad \text{with} \qquad \frac{1}{2} \leq \xi_R \leq 2 \tag{3}$$

where $\xi_R = 1$ is the default choice. Events are separately generated for each scale, and then plotted together using the central value as reference and the variation as error bars. For $t\bar{t}$ and $t\bar{t}H$ the top quarks are identified with the reconstructed jets containing a t quark. The jet reconstruction is carried out with the FastJet library [9], using the `ee-genKT` algorithm with $R = 0.4$ and $p = -1$.
For the on-shell $t\bar{t}$ and $t\bar{t}H$ processes, the decay widths are set to zero, falling back to the on-shell scheme.

2.3. Input parameters and cuts

For QCD NLO corrections, the method used for amplitude calculation is OpenLoops, which only supports massless muons in the initial state; for EW NLO correction Recola is used, in which the mass of the muon is set different from zero. The input parameters are here reported, taken from the latest PDG report [10]

- **Bosons Masses**
  - $M_W = 80.377\,\text{GeV}$
  - $M_Z = 91.1876\,\text{GeV}$
  - $M_H = 125.25\,\text{GeV}$
- **Quarks Masses**
  - $m_u = m_d = m_s = m_c = 0$
  - $m_b = 4.18\,\text{GeV}$
  - $m_t = 172.69\,\text{GeV}$
- **Leptons Masses**
  - $m_e = 0$
  - $m_\mu = 105.6\,\text{MeV}$
  - $m_\tau = 1.777\,\text{GeV}$

The calculation of W and t decay widths is done with WHIZARD, both at LO and NLO, generating the matrix elements with OPENLOOPS and then given as input for the event generation. For the W boson the computation is done at the scale equal to the boson mass, considering both leptonic $W \to l\nu$ and hadronic $W \to q\bar{q}'$ decays. The results, obtained as the sum of the two decay channels widths is

$$\Gamma_W^{\mathrm{LO}} = 2.044\,857\,\mathrm{GeV} \qquad \Gamma_W^{\mathrm{NLO}} = 2.097\,283\,\mathrm{GeV} \tag{4}$$

For the top width the on-shell $t \to W^+ b$ is taken in consideration.

$$\Gamma_t^{\mathrm{LO}} = 1.483\,314\,\mathrm{GeV} \qquad \Gamma_t^{\mathrm{NLO}} = 1.355\,064\,\mathrm{GeV} \tag{5}$$

In the off-shell calculations the NLO width is used, while for the top quark the order of the width matches the one of the calculation.
No phase-space cut is applied, as in principle the on-shell processes can be integrated over the total phase space. The beam is considered without a structure, but further study can take into consideration the realistic assumption of the gaussian spread of the muon beams energy, whereas it is causing problems to the parallelisation of the WHIZARD integration.

3. Phenomenology

The processes studied in this work are the on- and off- shell top-quark pair production, with an eventual associated emission of a Higgs boson. Since the BR of the top quark decay into a bottom quark and a weak gauge boson is almost 1, the off-shell process is the $t\bar{t}(H)$ production with the subsequent decay of the tops. In this section the phenomenology of both processes is presented. In particular in section 3.1, the $t\bar{t}$ production and decay is presented, while the section 3.2 will deal with top-quark pair production with an associated Higgs boson.

3.1. $t\bar{t}$ production and decay phenomenology

This section aims to give a brief phenomenological description of the following $2 \to 2$ and $2 \to 4$ processes considered

$$\mu^+\mu^- \to t\bar{t} \tag{6}$$
$$\mu^+\mu^- \to W^+W^-b\bar{b} \tag{7}$$

For the on-shell $t\bar{t}$ production both NLO QCD and EW corrections are being studied, while for the off-shell process only the QCD NLO perturbative corrections are taken into account. Bottom quarks are treated as massive. The LO Feynman amplitude for the electroweak process $\mu^+\mu^- \to t\bar{t}$ is given by the sum of the diagrams with the exchange of a photon and the one with a neutral weak Z boson, as shown in Figure 3.1 For the

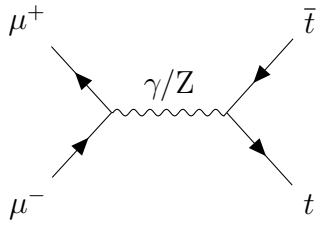

Figure 1: Feynman diagram(s) for $t\bar{t}$ production at LO.

Figure 2: Feynman diagrams for real (left) and virtual (right) gluon emission for $t\bar{t}$ production at NLO.

real QCD corrections to on-shell $t\bar{t}$ production, a gluon can be radiated only by the top or the antitop, while for EW corrections also the initial states can radiate a photon. In this case, the possible loop diagrams are only two, corresponding to a virtual emission and absorption of a gluon by one top, or between the top pair. Examples of the real and virtual loop diagrams for this process are shown in figure 3.1

Since the top quark decays almost exclusively via the $t \to W^{=}b$ channel, the off-shell process considered is the one in eq. 7. This process also receives background contributions from single resonant diagrams, in which only one top quark decays, and from a non-resonant diagram, where the final state signature is produced by vector bosons decays. Thanks to the finite bottom mass, vector boson splittings, such as $\gamma \to b\bar{b}$ occurring in the top right diagram of figure 3.1 can be integrated over the whole phase space without cuts. The calculation of the off-shell decay process contains non-factorisable corrections, i.e. a gluon connecting the two bottoms, or the top and the bottom quarks, of the order of $\mathcal{O}(\alpha_s \Gamma_t / m_t)$.

3.1.1. Forward Backward asymmetry

Due to the Z weak coupling, an asymmetry is present in the matrix element squared of the $t\bar{t}$ process. In fact, the calculation of the differential cross section w.r.t the angle between the top quark and the muon beam leads to

$$\frac{\mathrm{d}\sigma}{\mathrm{d}\cos\theta_t} = \frac{3\pi\alpha_e}{2s}\sqrt{1-\frac{4m_t^2}{s}}\left[F_1(s)(1+\cos^2\theta_t) + \frac{4m_t^2}{s}F_2(s)\sin^2\theta_t + \sqrt{1-\frac{4m_t^2}{s}}F_3(s)2\cos\theta_t\right] \tag{8}$$

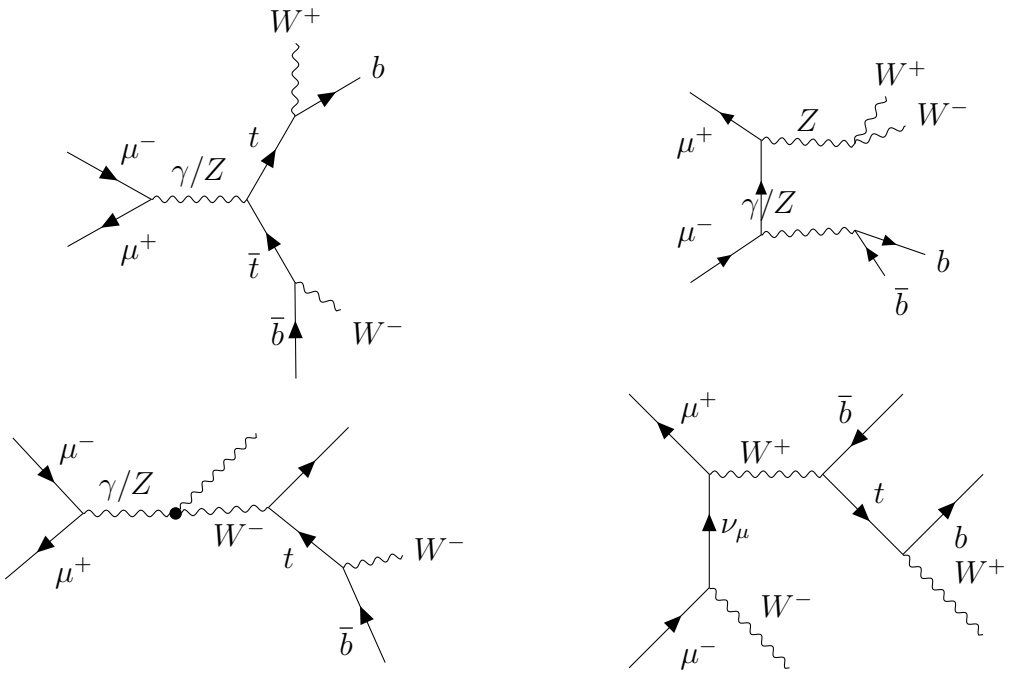

Figure 3: Feynman diagrams for LO off-shell top-pair production and decay. The top-left diagram is the only double resonant production, while the top-right one is the non-resonant. The bottom diagrams are the single resonant contributions.

where the functions $F_i(s), i = 1, 2, 3$ are related to the couplings and propagator factors, reported in appendix A. The cross section is asymmetric for $\theta_t \to -\theta_t$ due to the third therm of the r.h.s. of 31 proportional to $\cos\theta_t$. Hence one can define a measure of the asymmetry as the difference between the integrated cross section in the phase space region where $\cos\theta_t > 0$ with the one where $\cos\theta_t < 0$ normalized to the total cross section

$$A_{\rm FB} = \frac{\sigma_F - \sigma_B}{\sigma_F + \sigma_B}$$

where

$$\sigma_F = \int_0^1 \frac{\mathrm{d}\sigma}{\mathrm{d}\cos\theta}\, d\cos\theta, \qquad \sigma_B = \int_{-1}^0 \frac{\mathrm{d}\sigma}{\mathrm{d}\cos\theta}\, d\cos\theta \tag{9}$$

This quantity, usually called Forward Backward asymmetry, can be used to determine the effective weak mixing angle $\sin\theta_W^{\rm eff}$. Moreover, a future very precise measurement of the FB asymmetry achieved at a muon collider could be used as a probe for new physics, since various BSM predictions deviate from the SM predicted value [11].

3.2. $t\bar{t}H$ production and decay

The associated-Higgs boson top pair production is a $2 \to 3$ process

$$\mu^+\mu^- \to t\bar{t}H \tag{10}$$

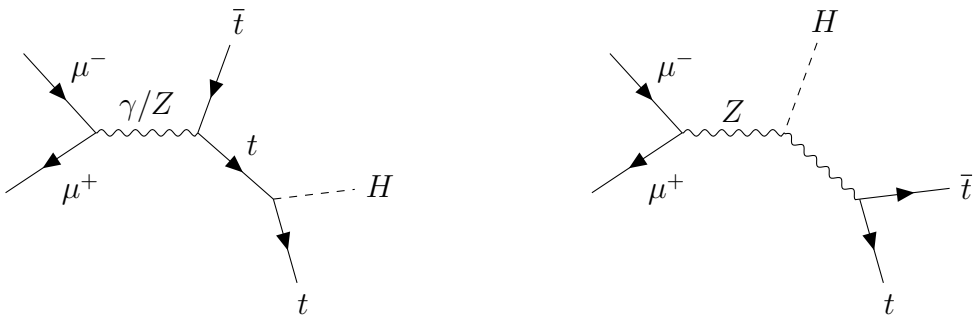

Figure 4: Feynman diagrams for associated Higgs boson top pair production at LO.

whose Feynman diagrams are similar to the corresponding $t\bar{t}$ process, with the addition of a Higgs boson emission from either the top or the antitop quark, or the intermediate massive weak boson. In figure 3.2 the diagrams for the process in eq 3.2 are depicted. The left one is proportional to the top Yukawa coupling y_t and for this analysis is the only contribution to the signal S. The rightmost diagram, on the other hand, represents the Higgsstrahlung from the intermediate Z boson and is the irreducible background source to $t\bar{t}H$ process.

3.2.1. Top Yukawa Coupling

In the Standard Model the Higgs boson couples to massive fermions via the Yukawa coupling, with a strength proportional to the mass m_f of the particle. The Yukawa interaction Lagrangian is

$$\mathcal{L}_{\text{Yuk}} = \frac{\sqrt{2}m_f}{v}\phi\overline{\psi_f}\psi_f \tag{11}$$

where ϕ is the Higgs field, and ψ_f is the Dirac field of the fermion, while v is the vacuum expectation value of the Higgs field, which in this setup reads $v = 246.219\,\text{GeV}$. Therefore, a precise measurement of the Higgs-associated top pair production translates into a precise and direct determination of the coupling between the Higgs field and the top quark. Since BSMs predict big deviation from the standard model top Yukawa coupling $y_t = \frac{\sqrt{2}m_t}{v} = 0.99$ and its measurement with a precision of few per cent can be a probe for new physics. The per cent measurement of the cross section of both on- and off-shell $t\bar{t}H$ processes can be achieved at a future muon collider. In the following section, the numerical results for y_t will be presented.

4. Results for inclusive cross sections

This section deals with all the numerical predictions obtained in this study with the calculation settings as described above. Firstly, the results for integrated cross sections are presented. Then, the subsequent subsections will show the Top Yukawa coupling computation results and the Forward Backward asymmetry.

4.1. Cross section and scale variation

In this subsection, the numerical results for the integrated cross section with both NLO QCD and EW corrections, and the QCD renormalization scale variation are reported.

4.1.1. Top pair production and decay

QCD corrections In the first place the calculation of the inclusive cross section for the on shell $t\bar{t}$ process is reported as a function of the centre-of-mass energy $\sqrt{s}$ of the muon beams.

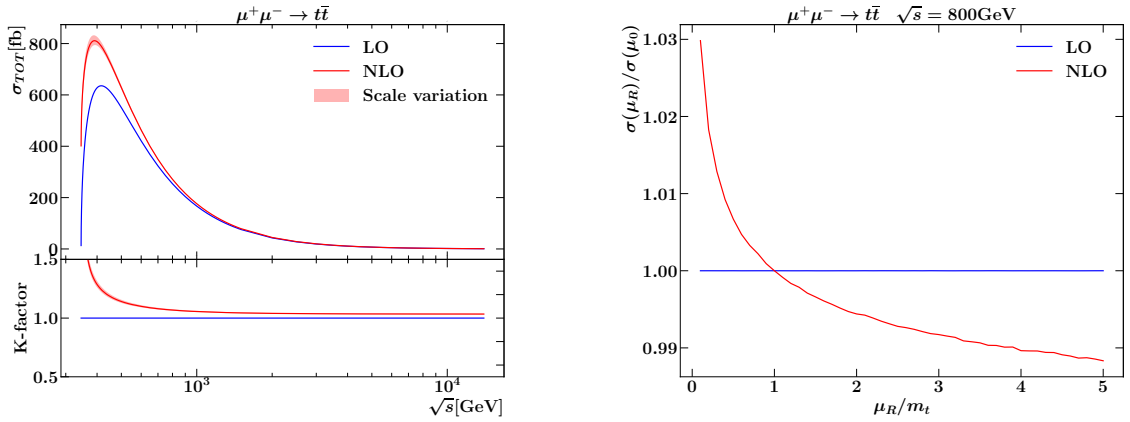

Figure 5: NLO QCD corrections to top pair production. To the left, the inclusvie cross section is plotted versus the centre of mass energy. The right plot shows the variation of the cross section, at a fixed value of s, as a function of the renormalisation scale. LO predictions in blue, NLO in red.

As can be seen in figure 4.1.1 the cross section is peaked right above the top-pair production threshold $s_{\text{thr}} = \sqrt{2m_t}$. The plot also shows the K-factor, which is the ratio between the NLO and LO cross sections.

$$K = \frac{\sigma^{\text{NLO}}}{\sigma^{\text{LO}}} \tag{12}$$

The NLO QCD cross section diverges as the energy approaches the top-pair threshold. This is due to the small kinetic energy of the non-relativistic top quarks, for which the strong coupling explodes. At very high energies, the NLO QCD corrections become negligible and both the LO and NLO cross sections fall proportionally to $1/s$. In table 4.1.1 the numerical results for some centre of mass energies are shown. While for energies right above the threshold QCD NLO corrections are around 10%, at the tera scale they become negligible. This is because at very high energies the top mass becomes negligible along with its effects, and the corrections approach to α_S/π, the universal correction factor for leptonic massless quark pair production. In the right panel of figure 4.1.1 shows how the cross section at $\sqrt{s} = 800\,\text{GeV}$ varies versus the renormalization scale ratio to

	$\mu^+\mu^- \to t\bar{t}$			$\mu^+\mu^- \to W^+W^-b\bar{b}$		
$\sqrt{s}$[GeV]	σ^{LO}[fb]	σ^{NLO}[fb]	$K_{\rm QCD}$	σ^{LO}[fb]	σ^{NLO}[fb]	$K_{\rm QCD}$
500	550.617	$628.381^{+1.32\%}_{-1.04\%}$	1.141	584.276	$675.183^{+0.09\%}_{-3.09\%}$	1.155
800	253.947	$271.310^{+0.65\%}_{-0.55\%}$	1.068	302.177	$325.842^{+0.57\%}_{-3.24\%}$	1.078
1000	166.794	$176.113^{+0.54\%}_{-0.44\%}$	1.055	211.424	$227.377^{+0.84\%}_{-4.55\%}$	1.075
1400	86.806	$90.759^{+0.48\%}_{-0.37\%}$	1.045	123.523	$125.811^{-2.40\%}_{-7.02\%}$	1.018
3000	19.180	$19.892^{+0.38\%}_{-0.32\%}$	1.037	37.242	$33.711^{-2.11\%}_{-12.77\%}$	0.905
6000	4.808	$4.977^{+0.38\%}_{-0.27\%}$	1.034	12.786	$9.297^{+11.09\%}_{-3.27\%}$	0.727
10000	1.732	$1.792^{+0.36\%}_{-0.29\%}$	1.034	5.854	$3.548^{+16.61\%}_{-30.50\%}$	0.606
14000	0.883	$0.914^{+0.36\%}_{-0.29\%}$	1.034	3.494	$2.635^{-2.21\%}_{-14.05\%}$	0.754

Table 1: LO and NLO QCD predictions for the total inclusive cross section for on-shell top pair production. The errors refer to the scale variation interval $[1/2m_t, 2m_t]$.

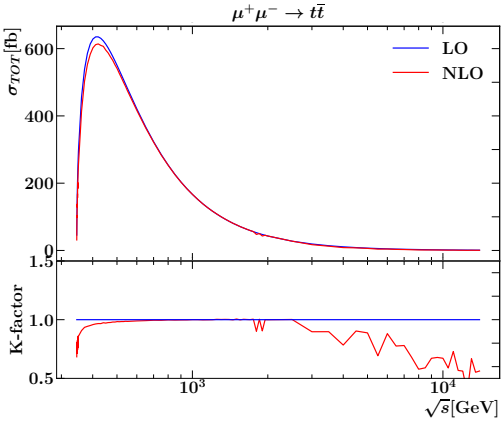

Figure 6: NLO EW corrections to on-shell top pair production

the top mass. Here, the central value is set as $\mu_0 = m_t$; the plot shows that as the scale increases, the cross section tends to be smaller. This translates into the error bands of the integrated cross section. The effect is however small and no significant deviations from the central value are present, as the variations are below the per cent.

EW corrections For electroweak corrections the initial-state muons are treated as massive to avoid divergences for the initial state radiation. In figure 4.1.1 the inclusive cross section for $t\bar{t}$ production is shown as a function of the centre of mass energy. Conversely to the QCD correction, the EW NLO correction is negative, so the NLO cross section turns out to be smaller than the LO one. Approaching the top pair threshold, the EW NLO cross section gets smaller and smaller. At very high energies, the K factor shows irregular behaviour, probably for flaws in the parallelised integration. The negative sign

of the electroweak corrections can be understood as the prevalence of the negative DL contributions, see [12]. At $\sqrt{s} = 1\,\text{TeV}$ the NLO cross section is very similar to the LO one, as the K factor becomes ~ 1. This can be understood as compensation between the double and single logarithmic corrections, which are of the same order of magnitude but with opposite signs. In table 4.1.1 the results of the integrated cross section for

$\mu^+\mu^- \to t\bar{t}$			
$\sqrt{s}$[GeV]	σ^{LO}[fb]	σ^{NLO}[fb]	K
500	550.6249	486.2882	0.883157
800	253.9514	227.7632	0.8968772
1000	166.798	166.9095	1.000669
1400	86.80873	69.65877	0.8024398
3000	19.18138	13.42351	0.6998198
6000	4.809052	1.453612	0.3022659
10000	1.732296	0.6740623	0.3891149
14000	0.8839725	0.3358422	0.3799238

Table 2: LO and NLO EW corrections to on-shell top pair production.

some standard $\sqrt{s}$ values are reported.

4.1.2. Higgs associated top pair production

The inclusive cross section for $t\bar{t}H$ is shown in figure 4.1.2. In this case, the peak is at $\sqrt{s} \sim 800\,\text{GeV}$, while the production threshold is sat $2m_t + m_H \sim 470.9\,\text{GeV}$ Also in this

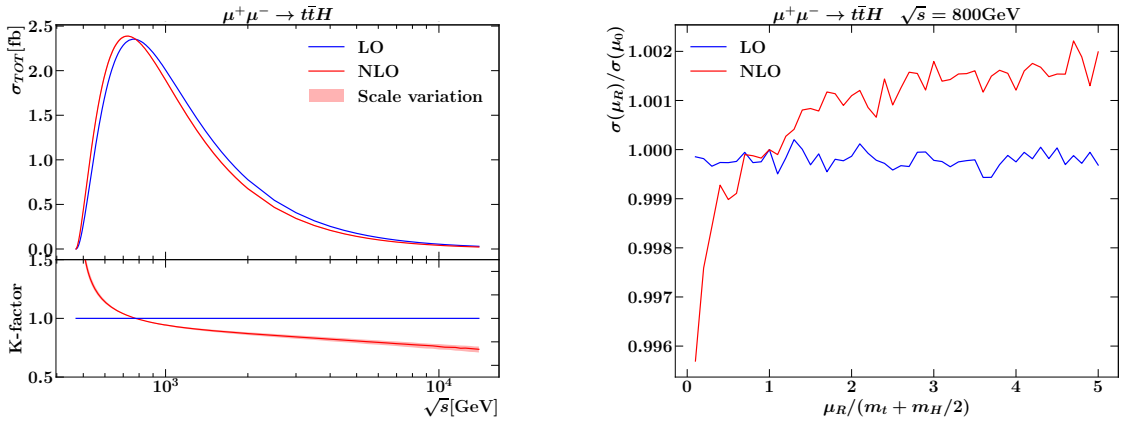

Figure 7: NLO QCD corrections to top pair production with an associated Higgs boson. Panels as in figure 4.1.1

case the corrections are bigger near the threshold, being around +60% at $\sqrt{s} = 500\,\text{GeV}$, but after being around the per cent at the peak, they turn negative, reaching −17% at

the highest energy studied. On the other hand, scale variation is totally negligible for this process. In table 4.1.2 the numerical results for the on shell process are listed. In

	$\mu^+\mu^- \to t\bar{t}H$		
$\sqrt{s}$[GeV]	σ^{LO}[fb]	σ^{NLO}[fb]	K
500	0.272	$0.435^{+3.82\%}_{-3.13\%}$	1.601
800	2.339	$2.319^{+0.01\%}_{-0.09\%}$	0.991
1000	2.008	$1.893^{+0.49\%}_{-0.62\%}$	0.942
1400	1.323	$1.192^{+0.81\%}_{-1.08\%}$	0.900
1000	2.009	$1.894^{+0.45\%}_{-0.65\%}$	0.942
3000	0.406	$0.342^{+1.54\%}_{-1.84\%}$	0.842
6000	0.128	$0.102^{+2.22\%}_{-2.55\%}$	0.794
10000	0.053	$0.040^{+3.01\%}_{-3.11\%}$	0.759
14000	0.030	$0.0221^{+3.33\%}_{-3.13\%}$	0.735

Table 3: LO and NLO cross sections predictions with QCD corrections for associated Higgs boson top-pair production. Errors as before.

the next section the results for differential cross sections will be shown, taking as the centre of mass energy $\sqrt{s} = 800\,\text{GeV}$, for it is the energy value of the $t\bar{t}H$ cross section peak.

EW corrections The on-shell EW NLO corrections to $t\bar{t}H$ are sensibly bigger than the QCD ones, even at low energies. It is interesting to note that the sign of the corrections is negative in both the QCD and EW cases, except for $\sqrt{s} = 500\,\text{GeV}$.

	$\mu^+\mu^- \to t\bar{t}H$		
$\sqrt{s}$[GeV]	σ^{LO}[fb]	σ^{NLO}[fb]	K
500	0.271	0.091	0.335
800	2.339	1.533	0.655
1000	2.008	1.402	0.698
1400	1.323	0.967	0.731
1000	2.008	1.322	0.658
3000	0.407	0.296	0.728
6000	0.128	0.086	0.669
10000	0.053	0.027	0.516
14000	0.030	0.017	0.579

Table 4: EW NLO corrections for associated Higgs boson top-pair production.

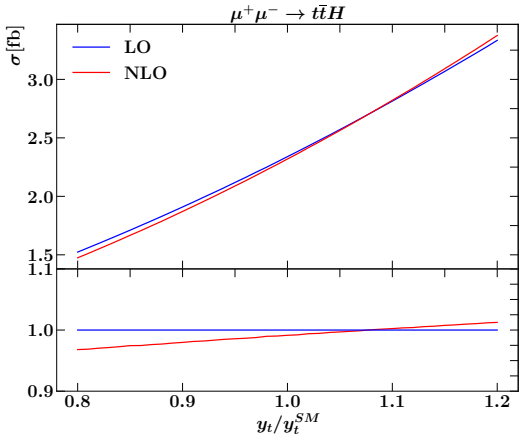

Figure 8: Cross section for $\mu^+\mu^- \to t\bar{t}H$ as a function of the top Yukawa coupling modifier $\xi_t = y_t/y_t^{\mathrm{SM}}$

4.2. Yukawa coupling

The sensitivity of the top pair production with an associated Higgs boson cross section, as described in section **??**, to the top Yukawa coupling can be expressed as

$$\frac{\Delta y_t}{y_t} = \kappa \frac{\Delta \sigma}{\sigma} \tag{13}$$

Defining the ratio between the top Yukawa coupling and its SM value as $\xi_t = y_t/y_t^{\mathrm{SM}}$, the relation 4.2 can be rewritten as

$$\frac{\mathrm{d}\sigma(\xi_t)}{\mathrm{d}\xi_t} = \frac{1}{\kappa}\frac{\sigma}{\xi_t} \tag{14}$$

Since the cross section depends approximately quadratically on the Yukawa coupling, one expects κ to be close to 0.5. For a more precise analysis, one can model the cross section as being made up by contribution from the signal S and from the background B, as well as their interference I (where S, I, B include the squared matrix elements for the signal, background and their interference as well as all other numerical factors and energy dependency). Hence, the cross section as a function of ξ_t reads

$$\sigma(\xi_t) = \xi_t^2 S + \xi_t I + B \tag{15}$$

and it is showed in figure 31 The sensitivity of the signal to y_t can be determined by a linear fit of the cross section as a function of ξ_t

$$\kappa = \lim_{\xi_t \to 1} \sigma(\xi_t) \left(\frac{\mathrm{d}\sigma(\xi_t)}{\mathrm{d}\xi_t} \right)^{-1} = \frac{S + I + B}{2S + I} = \frac{1}{2} + \frac{I/2 + B}{2S + I} \tag{16}$$

The κ parameter is extracted from the data doing a linear fit of the cross section as $\sigma(\xi_t) = a\xi_t + b$, taking the value for $\xi_t = 1$,

$$\kappa = \frac{1}{a}\frac{\sigma(\xi_t)}{\xi_t}\bigg|_{\xi_t=1} = \lim_{\xi_t \to 1} \left(\frac{\mathrm{d}\sigma(\xi_t)}{\mathrm{d}\xi_t} \right)^{-1} \sigma(\xi_t) \tag{17}$$

The deviation of the fitted parameter from 0.5 can be used to determine the background contribution, which is positive. While no assumption can be made on the sign of the interference term, it is safe to assume that the signal dominates over the interference, i.e. $-I < 2S$: in such way, $\kappa < 0.5$ can be obtained iff $I < -2B$. In table 4.2 the

$\mu^+\mu^- \to$		κ^{LO}	κ^{NLO}	$\kappa^{\text{NLO}}/\kappa^{\text{LO}}$
$t\bar{t}H$	QCD	0.517	0.488	0.944

Table 5: κ-parameter for on-shell top pair production

numerical predictions for the κ facotr for the on-shell process are reported. All the values are, as expected, close to 0.5. The LO value is bigger, and this can be understood as contribution from the backgrounding Higgsstrahlung process, where the Higgs boson is radiated by the intermediate Z boson. The around 6% correction for the QCD NLO can be understood as a different behavior for the signal and the background; the sign of the correction turns out to be negative.

5. Results for differential cross sections

In this section, differential cross sections plots will be displayed, to better understand the differences and similarities between $t\bar{t}$ and $t\bar{t}H$. Theoretically, as well as experimentally, the on-shell and off-shell processes (and the subsequent decay) are similar. Is it necessary to study the details of the top-pair production and decay, as a large amount of data could be experimentally collected by a muon collider, because it is the key to studying the top-Yukawa coupling and looking for new physics. Henceforth, all the predictions are calculated at a fixed centre of mass value $\sqrt{s} = 800\,\text{GeV}$. Both the NLO QCD and EW corrections for the on-shell $\mu^+\mu^- \to t\bar{t}(H)$ will be discussed, with also particular attention to the forward-backward asymmetry, previously introduced in section **??**.

5.1. $t\bar{t}$ production and decay

As previously mentioned, (anti)top quarks in the final state are identified as the reconstructed jets containing an (anti)top quark. For the off-shell process, the top and antitop quarks properties are reconstructed via the sum of the jets momenta of the decay products, W^+b and $W^-\bar{b}$, respectively.

QCD corrections At first, the on-shell top pair production differential distributions in the energy and p_T for the top quark are displayed in figure 5.1. The predictions for this process are very precise and the scale variations are negligible, at least for lower energies. At LO, the top energy has a trivial distribution peaked at $E_t = 400\,\text{GeV}$, which is the energy of the beam. At NLO, the differential distribution of the top quark is spread but

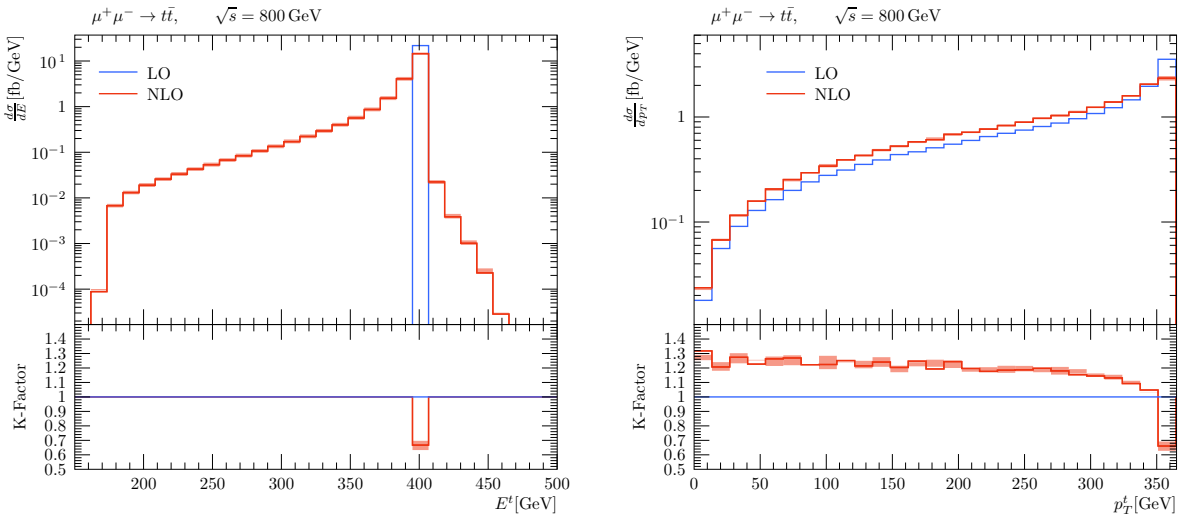

Figure 9: Differential distributions in E and p_T of the top quark for $\mu^+\mu^- \to t\bar{t}$.

still peaked at the same value: this is the effect of the real emission of the gluon. In figure 5.1, the same differential distributions are computed for the on-shell process with the subsequent decays. In this case, the top and antitop energies are reconstructed at the truth levels as $E_t = E_{W+j_b}$. The profile for these predictions is way less clear than the on-shell process, more statistics and integration calls are needed. However, a feature is visible, at least at LO: the energy distribution is not trivial because of the off-shellness of the top-quark pair. The peak in the transverse momentum distribution is due to

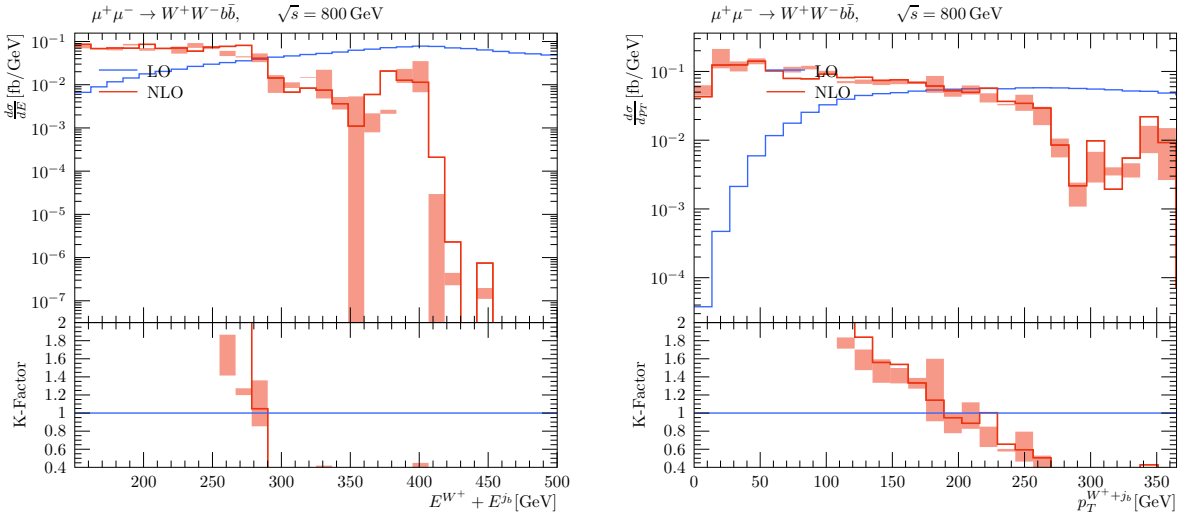

Figure 10: Differential distributions in E and p_T of the reconstructed top quark for $\mu^+\mu^- \to W^+W^-b\bar{b}$.

the Jacobian peak, i.e. the coordinate transformation from the cross section differential in the polar angle to the one differential in the transverse momentum. The transverse

momentum of the outgoing top quark is given by

$$p_T^t = (\sqrt{E_t^2 - m_t^2})\sin\theta \qquad \Rightarrow \qquad \cos\theta = \sqrt{1 - \frac{p_T^2}{E_t^2 - m_t^2}} \tag{18}$$

Hence, the Jacobian transformation reads

$$\frac{\mathrm{d}\sigma}{\mathrm{d}p_T} = \frac{\mathrm{d}\sigma}{\mathrm{d}\cos\theta_t}\frac{\mathrm{d}\cos\theta_t}{\mathrm{d}p_T} = \frac{\mathrm{d}\sigma}{\mathrm{d}\cos\theta_t}\frac{p_T}{\sqrt{E_t^2 - m_t^2}}\frac{1}{\sqrt{E_t^2 - m_t^2 - p_T^2}} \tag{19}$$

which peaks for $p_T = \sqrt{E_t^2 - m_t^2}$, which for the maximum energy $E_t = 400\,\mathrm{GeV}$, corresponds to approximately $360\,\mathrm{GeV}$, which is observed. Further NLO QCD predictions have been computed and will be reported in an appendix.

EW corrections The same differential distributions have been studied for the on-shell process with EW corrections, in this case the antitop predictions are displayed in figure 5.1. The general behaviour is basically the same.

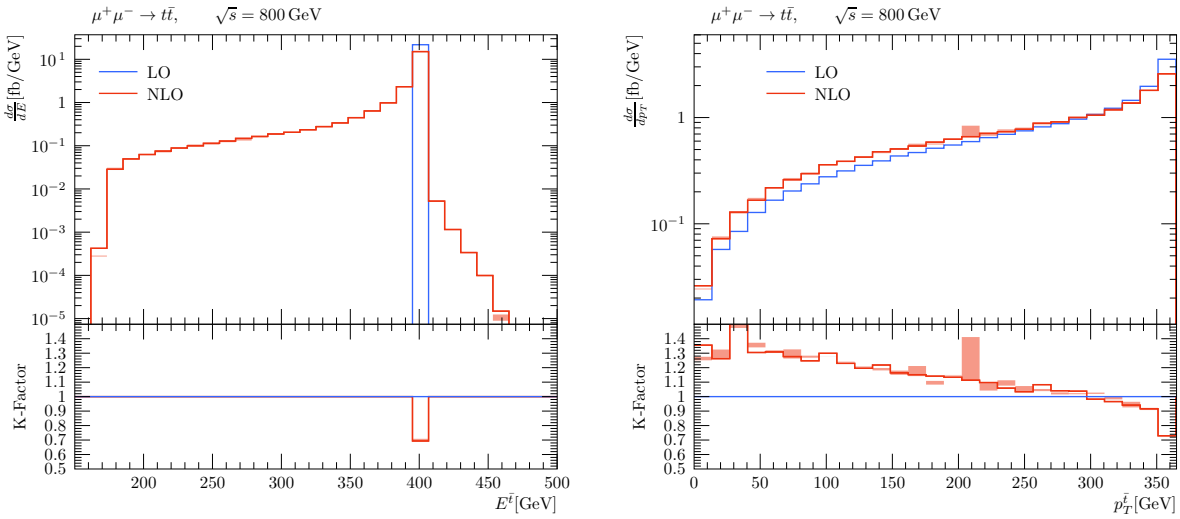

Figure 11: Differential distributions in E and p_T of the antitop quark for $\mu^+\mu^- \to W^+W^-b\bar{b}$.

5.2. Forward-Backward asymmetry

In figure 5.2 are reported the differential cross sections w.r.t the angle θ_t between the outgoing top quark and the incoming antimuon for the top pair production, with both QCD NLO and EW NLO corrections. As previously explained, the differential distribution is not symmetrical for $\theta_t \to -\theta_t$ and the usually-called forward-backward asymmetry quantity, as defined in 3.1.1, is a measure of this asymmetry. In table 6 the NLO QCD and EW corrections to the forward backward asymmetry of both the top and antitop

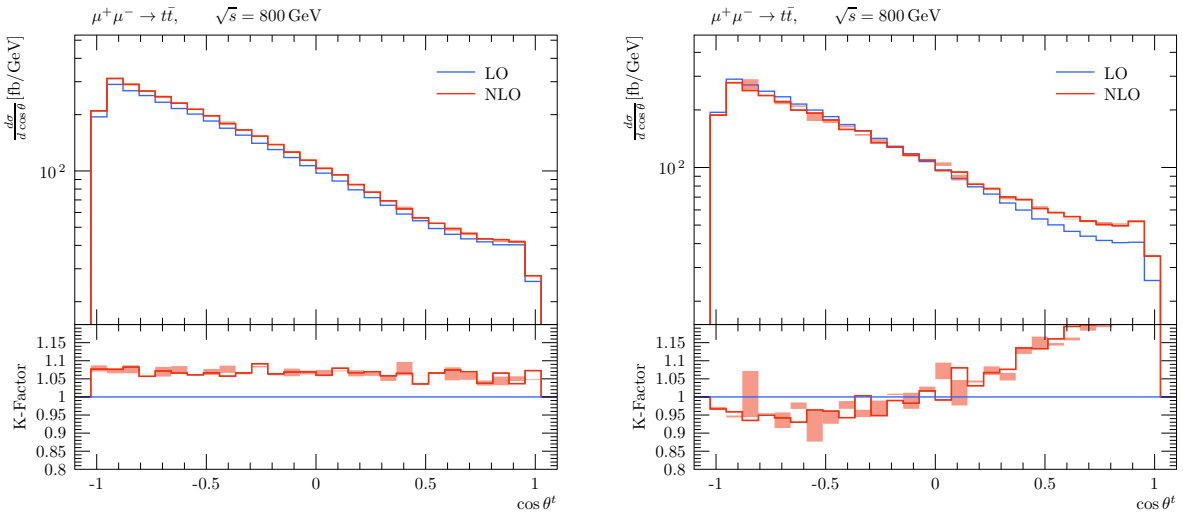

Figure 12: Differential distribution in the angle θ_t for top pair production, with QCD corrections (left panel) and EW (right panel). LO predictions in blue, NLO in red. The light red shaded area refers to the renormalization scale variation interval.

		$\mu^+\mu^- \to t\bar{t}$		
		$A_{\text{FB}}^{\text{LO}}$	$A_{\text{FB}}^{\text{NLO}}$	$A_{\text{FB}}^{\text{NLO}}/A_{\text{FB}}^{\text{LO}}$
A_{FB}	QCD	-0.536	-0.539	1.004
	EW	-0.535	-0.476	0.890
$\overline{A}_{\text{FB}}$	QCD	0.536	0.538	1.004
	EW	0.535	0.477	0.891

Table 6: Forward backward asymmetry calculation for the top (antitop) quark A_{FB} ($\overline{A}_{\text{FB}}$) for $\sqrt{s} = 800\,\text{GeV}$

polar angle are reported. As expected, since the only variation between the top and antitop differential cross sections in the azimuthal angle is the charge of the quark, the LO predictions are one the opposite of the other. At the NLO the antitop FB asymmetry is not exactly the opposite of the top one, but this small discrepancy can be attributed to the integration error. It is also noted that, while the QCD corrections account only for less than a half per cent, the EW corrections are more important, settling around -11%. The negative sign of the EW correction comes with no surprise for the same reasons as above; the larger size may be understood by the fact that the weak NLO left-handed diagrams generate large corrections. The same study has been done for the off-shell $\mu^+\mu^- \to W^+W^-b\bar{b}$ process, as displayed in table 7 It is noted that in this case the value is smaller and that the relation $A_{\text{FB}} = -\overline{A_{\text{FB}}}$ is not fulfilled at NLO. This can be attributed to uncertainties in the reconstruction of the final states but it is quite peculiar.

		$\mu^+\mu^- \to W^+W^-b\bar{b}$		
		$A_{\rm FB}^{\rm LO}$	$A_{\rm FB}^{\rm NLO}$	$A_{\rm FB}^{\rm NLO}/A_{\rm FB}^{\rm LO}$
$A_{\rm FB}$	QCD	-0.427	-0.466	1.091
$\overline{A}_{\rm FB}$	QCD	0.427	0.415	1.004

Table 7: Forward backward asymmetry calculation for the top (antitop) quark $A_{\rm FB}$ ($\overline{A}_{\rm FB}$) for $\sqrt{s} = 800\,\text{GeV}$

5.3. $t\bar{t}H$ production

The associated Higgs boson top pair production process gives the opportunity to study the properties of the top-pair threshold through the Higgs boson properties. The differential cross section w.r.t. the top energy has a non-trivial shape even at LO, due to the presence of the Higgs boson. In figure 5.3 and 5.3 the energy and transverse momentum of the top quark are plotted, with QCD and EW NLO corrections respectively.

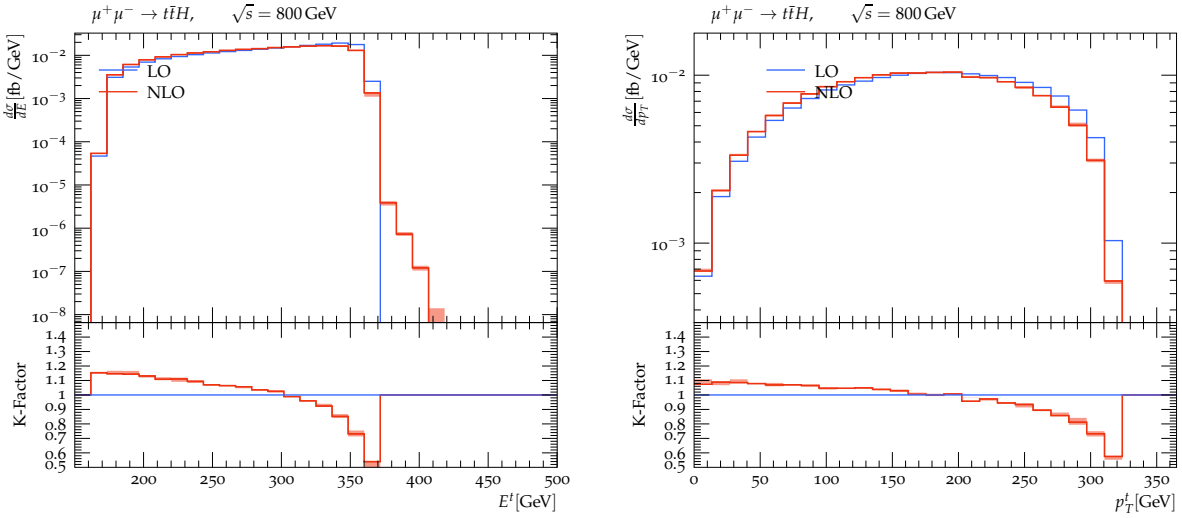

Figure 13: Differential distributions in E and p_T of the antitop quark for $\mu^+\mu^- \to t\bar{t}H$ with QCD corrections.

6. Conclusions

In this project, I have studied the NLO QCD and EW predictions to top pair production, also with an associated Higgs boson, for a future muon collider. For the first time, a complete treatment of the NLO QCD predictions has been presented for the on-shell processes $\mu^+\mu^- \to t\bar{t}$ and $\mu^+\mu^- \xrightarrow{t} \bar{t}$. NLO QCD corrections have been computed also for $\mu^+\mu^- \to W^+W^-b\bar{b}$. A partial treatment of the NLO EW corrections for $\mu^+\mu^- \to t\bar{t}$ and $\mu^+\mu^- \xrightarrow{t} \bar{t}$ has been achieved, although a deeper study is necessary.

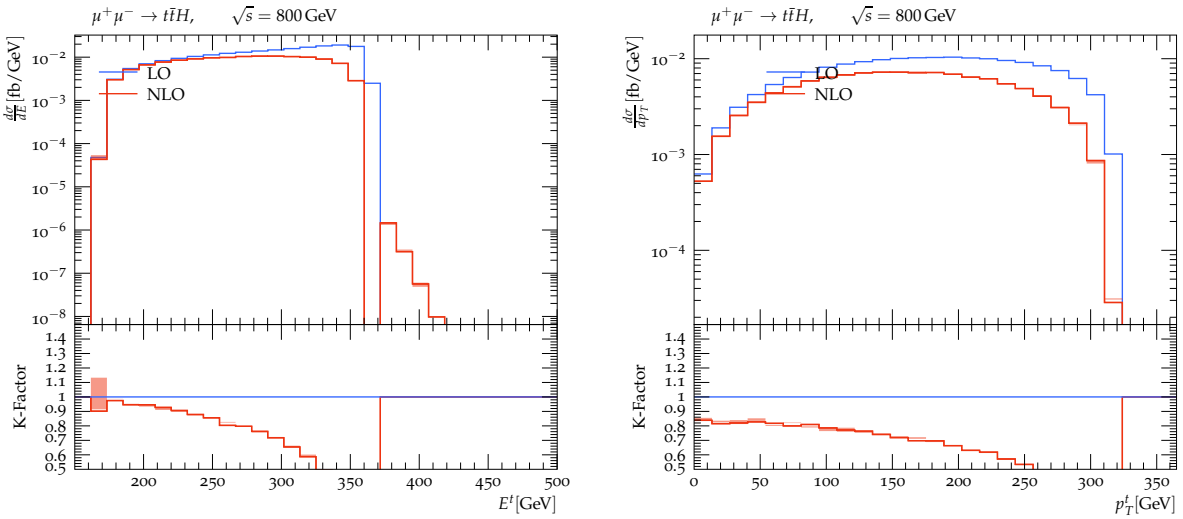

Figure 14: Differential distributions in E and p_T of the antitop quark for $\mu^+\mu^- \to t\bar{t}H$ with EW corrections.

The wide range of predictions given in this work covers different sets of analyses. In the first place, the inclusive total cross sections have been given as a function of the centre of mass energy. Moreover, the NLO QCD predictions dependency on the renormalisation scale has been probed, with accurate predictions. Then, predictions for the top Yukawa coupling are useful for a better understanding of the Higgs sector and the stability of the electroweak vacuum. Moreover, predictions for the forward-backwards asymmetry within the QCD and EW next to leading order frameworks are crucial for the determination of the effective weak mixing angle.
In particular, it has been shown that NLO QCD corrections can reach the order of tens per cent on various occasions and that the NLO EW corrections are even larger, but usually with an opposite sign.
In addition, differential distributions for a variety of quantities have been computed for multiple processes.
Nevertheless, a lot of work has to be done. Statistics need to be enhanced by scaling the number of events by at least a factor of 10. Moreover, NLO EW prediction needs to be further developed and validated, and NLO QCD predictions can be extended also to the process $\mu^+\mu^- \to \mu^+\nu_\mu e^-\overline{\nu}_\mu b\bar{b}(H)$ with the actual settings.

Acknowledgments

I want to thank my supervisor Jürgen Reuter for giving me the opportunity to work on this on-site project in the beautiful and stimulating research centre that DESY is. I also want to thank Pia Bredt for the almost daily help and support she gave me, always with kindness. I whish to thank Pascal Stienemeier for his precise and precious support even for technical questions.
This project has been done within the DESY Summer Students 2022 program, which I

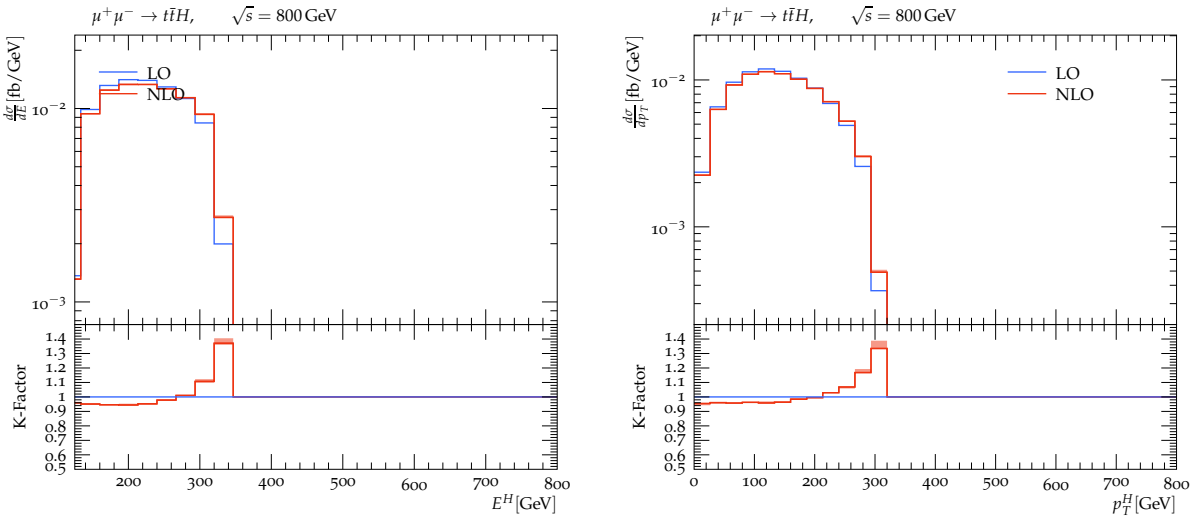

Figure 15: Differential distributions in E_H and p_T^H of the Higgs boson for $\mu^+\mu^- \to t\bar{t}H$ with QCD corrections.

think is an unmissable opportunity for students like me to approach the research world and touch it with hand.

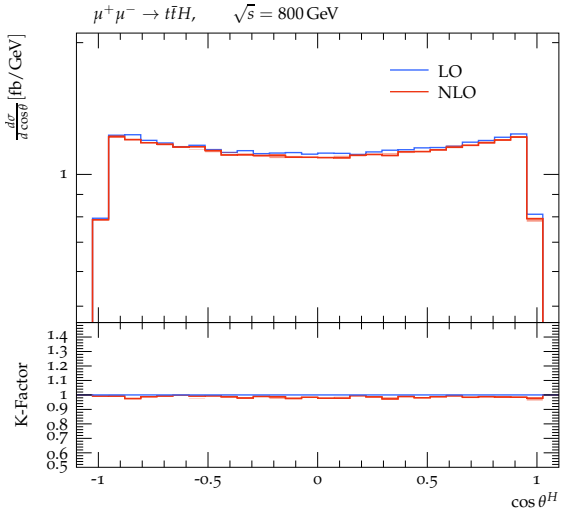

Figure 16: Differential distributions in $\cos\theta_H$ for $\mu^+\mu^- \to t\bar{t}H$ with QCD corrections.

References

[1] Chiara Aime et al. "Muon Collider Physics Summary". In: (Mar. 2022). arXiv: 2203.07256 [hep-ph].

[2] Bijan Chokoufé Nejad et al. "NLO QCD predictions for off-shell tt and ttH production and decay at a linear collider". In: *Journal of High Energy Physics* 2016.12 (Dec. 2016). DOI: 10.1007/jhep12(2016)075. URL: https://doi.org/10.10072Fjhep1228201629075.

[3] Wolfgang Kilian, Thorsten Ohl, and Jürgen Reuter. "WHIZARD—simulating multi-particle processes at LHC and ILC". In: *The European Physical Journal C* 71.9 (Sept. 2011). DOI: 10.1140/epjc/s10052-011-1742-y. URL: https://doi.org/10.1140%2Fepjc%2Fs10052-011-1742-y.

[4] Mauro Moretti, Thorsten Ohl, and Juergen Reuter. *O'Mega: An Optimizing Matrix Element Generator*. 2001. DOI: 10.48550/ARXIV.HEP-PH/0102195. URL: https://arxiv.org/abs/hep-ph/0102195.

[5] S. Actis et al. "Recursive generation of one-loop amplitudes in the Standard Model". In: *Journal of High Energy Physics* 2013.4 (Apr. 2013). DOI: 10.1007/jhep04(2013)037. URL: https://doi.org/10.1007%2Fjhep04%282013%29037.

[6] Andy Buckley et al. "Rivet user manual". In: *Computer Physics Communications* 184.12 (Dec. 2013), pp. 2803–2819. DOI: 10.1016/j.cpc.2013.05.021. URL: https://doi.org/10.1016%2Fj.cpc.2013.05.021.

[7] A. Denner et al. "Electroweak corrections to charged-current fermion processes: Technical details and further results". In: *Nuclear Physics B* 724.1-2 (Sept. 2005), pp. 247–294. DOI: 10.1016/j.nuclphysb.2005.06.033. URL: https://doi.org/10.1016%2Fj.nuclphysb.2005.06.033.

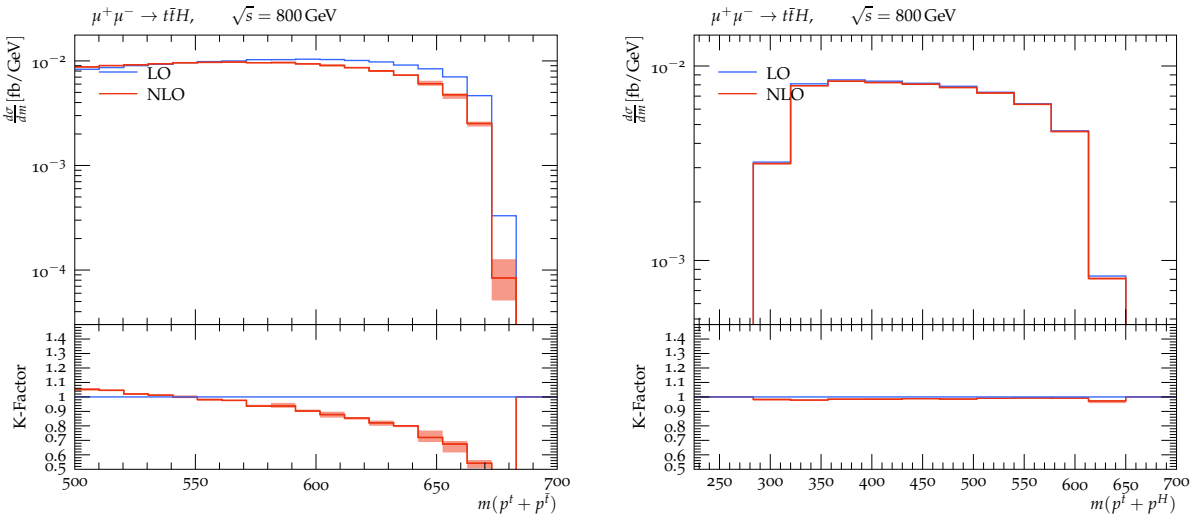

Figure 17: Top-antitop and top-Higgs invariant mass for $\mu^+\mu^- \to t\bar{t}H$ with QCD corrections.

[8] A. Denner and S. Dittmaier. "The complex-mass scheme for perturbative calculations with unstable particles". In: *Nuclear Physics B - Proceedings Supplements* 160 (Oct. 2006), pp. 22–26. DOI: 10.1016/j.nuclphysbps.2006.09.025. URL: https://doi.org/10.1016%2Fj.nuclphysbps.2006.09.025.

[9] Matteo Cacciari, Gavin P. Salam, and Gregory Soyez. "FastJet user manual". In: *The European Physical Journal C* 72.3 (Mar. 2012). DOI: 10.1140/epjc/s10052-012-1896-2. URL: https://doi.org/10.1140%2Fepjc%2Fs10052-012-1896-2.

[10] R. L. Workman et al. "Review of Particle Physics". In: *PTEP* 2022 (2022), p. 083C01. DOI: 10.1093/ptep/ptac097.

[11] Francois Richard. *Present and future constraints on top EW couplings*. 2014. DOI: 10.48550/ARXIV.1403.2893. URL: https://arxiv.org/abs/1403.2893.

[12] Ansgar Denner and Stefano Pozzorini. "One loop leading logarithms in electroweak radiative corrections. 1. Results". In: *Eur. Phys. J. C* 18 (2001), pp. 461–480. DOI: 10.1007/s100520100551. arXiv: hep-ph/0010201.

A. Appendix A

This appendix will show a more detailed calculation of the cross section. At the leading order, the process $\mu^+\mu^- \to t\bar{t}$ can both happen via the exchange of a photon or a massive neutral Z boson. Hence, there are two Feynman diagrams contributing

$$|\mathcal{M}|^2 = |\mathcal{M}_\gamma + \mathcal{M}_Z|^2 = \Bigg|$$

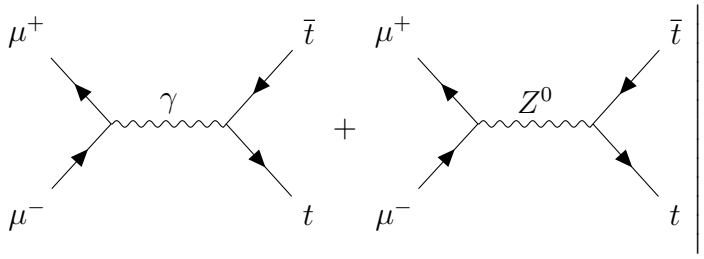

$$\Bigg|^2$$

where, since we put $\Gamma_Z = 0$,

$$\mathcal{M}_\gamma = -i4\pi\alpha_e Q_t(\overline{u}_t\gamma^\nu v_t)\frac{g_{\rho\nu}}{q^2}(\overline{v}_\mu\gamma^\rho u_\mu) \tag{20}$$

$$\mathcal{M}_Z = -i\sqrt{2}G_F M_Z^2[\overline{u}_t\gamma^\nu(c_V^t - c_A^t\gamma^5)v_t]\frac{g_{\rho\nu} - q_\rho q_\nu/M_Z^2}{q^2 - M_Z^2}[\overline{v}_\mu\gamma^\rho(c_V^\mu - c_A^\mu\gamma^5)u_\mu] \tag{21}$$

The factors c_V^f and c_A^f are the vector and axial weak coupling, respectively

$$c_V^f = I_3^f - 2Q_f\sin^2\theta_W, \qquad c_A = I_3^f \tag{22}$$

Hence, the matrix element squared averaged over spins is

$$|\mathcal{M}|^2 = \frac{1}{4}\sum_{\text{spins}}|\mathcal{M}_\gamma + \mathcal{M}_Z|^2 = \frac{1}{4}\sum_{\text{spins}}\left(\mathcal{M}_\gamma\overline{\mathcal{M}}_\gamma + 2\mathcal{M}_\gamma\overline{\mathcal{M}}_Z + \mathcal{M}_Z\overline{\mathcal{M}}_Z\right) \tag{23}$$

$$\mathcal{M}_\gamma\overline{\mathcal{M}_\gamma} = |A|^2 g_{\rho\nu}g_{\lambda\sigma}X_\mu^{\rho\lambda}X_t^{\sigma\nu} \tag{24}$$

$$\mathcal{M}_\gamma\overline{\mathcal{M}_Z} = A\overline{B}\left(g_{\rho\nu}g_{\lambda\sigma} - \frac{g_{\rho\nu}q_\lambda q_\sigma}{M_Z^2}\right)T_\mu^{\rho\lambda}T_t^{\sigma\nu} \tag{25}$$

$$\mathcal{M}_Z\overline{\mathcal{M}_Z} = |B|^2\left(g_{\rho\nu}g_{\lambda\sigma} - 2\frac{g_{\rho\nu}q_\lambda q_\sigma}{M_Z^2} + \frac{q_\rho q_\nu q_\lambda q_\sigma}{M_Z^4}\right)K_\mu^{\rho\lambda}K_t^{\sigma\nu} \tag{26}$$

Where the fermionic lines traces are defined as

$$X_f^{\rho\lambda} = \text{Tr}\left[\gamma^\rho u_f\overline{u}_f\gamma^\lambda v_f\overline{v}_f\right] \tag{27}$$

$$T_f^{\rho\lambda} = \text{Tr}\left[\gamma^\rho u_f\overline{u}_f\gamma^\lambda(c_V^f - c_A^f\gamma^5)v_f\overline{v}_f\right] \tag{28}$$

$$K_f^{\rho\lambda} = \text{Tr}\left[\gamma^\rho(c_V^f - c_A^f\gamma^5)u_f\overline{u}_f\gamma^\lambda(c_V^f - c_A^f\gamma^5)v_f\overline{v}_f\right] \tag{29}$$

Using the following expression for the differential cross section, neglecting the muon mass,

$$\frac{\mathrm{d}\sigma}{\mathrm{d}\Omega} = \frac{1}{64\pi^2 s}\frac{\sqrt{s-4m_t^2}}{2\sqrt{s}}|\mathcal{M}|^2, \qquad \frac{\mathrm{d}\sigma}{\mathrm{d}\cos\theta} = \int d\phi\frac{\mathrm{d}\sigma}{\mathrm{d}\Omega} \tag{30}$$

the differential cross section with respect the angle between to the angle between the top quark and the antimuon reads

$$\frac{\mathrm{d}\sigma}{\mathrm{d}\cos\theta_t} = \frac{3\pi\alpha_e}{2s}\sqrt{1-\frac{4m_t^2}{s}}\left[F_1(s)(1+\cos^2\theta_t) + \frac{4m_t^2}{s}F_2(s)\sin^2\theta_t + \sqrt{1-\frac{4m_t^2}{s}}F_3(s)2\cos\theta_t\right] \tag{31}$$

where the "Form factors" are defined as

$$F_1 = Q_t^2 - W2c_V^\mu c_A^\mu Q_t \mathrm{Re}[\chi(s)] + W^2\{[(c_V^\mu)^2+(c_A^\mu)^2][(c_V^t)^2+(c_A^t)^2] - \frac{4m_t^2}{s}(c_A^t)^2\}|\chi(s)|^2 \tag{32}$$

$$F_2 = Q_t^2 - W2c_V^\mu c_A^\mu Q_t \mathrm{Re}[\chi(s)] + W^2\{[(c_V^\mu)^2+(c_A^\mu)^2][(c_V^t)^2+(c_A^t)^2] - \frac{4m_t^2}{s}(c_A^t)^2\}|\chi(s)|^2 \tag{33}$$

$$F_3 = -W2c_A^\mu c_A^t Q_t \mathrm{Re}[\chi(s)] + W^2 4c_V^\mu c_A^\mu c_V^t c_A^t |\chi(s)|^2 \tag{34}$$

with

$$W = \frac{\sqrt{2}G_F M_Z^2}{4\pi\alpha_e} \tag{35}$$